

Contents lists available at ScienceDirect

Journal of Magnetic Resonance

journal homepage: www.elsevier.com/locate/jmr



RF atomic magnetometer array with over 40 dB interference suppression using electron spin resonance



Robert J. Cooper, David W. Prescott, Garrett J. Lee, Karen L. Sauer*

Department of Physics and Astronomy, George Mason University, Fairfax, VA, 22030, United States

ARTICLE INFO

Article history:
Received 21 June 2018
Revised 23 August 2018
Accepted 23 August 2018
Available online 28 August 2018

Keywords:
Electron spin resonance
Atomic magnetometer array
RF magnetic field mapping
Unshielded detection
Interference rejection
Low-field magnetic resonance

ABSTRACT

An unshielded array of 87 Rb atomic magnetometers, operating close to 1 MHz, is used to attenuate interference by 42–48 dB. A sensitivity of 15 fT/ $\sqrt{\text{Hz}}$ to a local source of signal is retained. In addition, a 2D spectroscopic technique, in which the magnetometers are repeatedly pumped and data acquired between pump times, enables a synchronously generated signal to be distinguished from an interfering signal very close in frequency; the timing and signal mimics what would be observed in a magnetic resonance echo train. Combining the interference rejection and the 2D spectroscopy techniques, a 100 fT local signal is differentiated from a 20 pT interference signal operating only 1 Hz away. A phase-encoded reference signal is used to calibrate the magnetometers in real time in the presence of interference. Key to the strong interference rejection is the accurate calibration of the reference signal across the array, obtained through electron spin resonance measurements. This calibration is found to be sensitive to atomic polarization, RF pulse duration, and direction of the excitation. The experimental parameters required for an accurate and robust calibration are discussed.

© 2018 Elsevier Inc. All rights reserved.

1. Introduction

In recent years, atomic magnetometers have become increasingly popular, with particular attention on applications in medical fields [1–7] such as magnetocardiography [8–10] and magnetoencephalography [11,12], in geomagnetics [13,14], and even in the search for axions and axion-like particles (ALPs) through the GNOME collaboration [15–17]. The atomic magnetometers rival the sensitivity of super-conducting quantum interference device (SQUID) magnetometers [18,19], but do not require cryogenic temperatures to operate. Many groups are also working on miniaturizing atomic magnetometers [20,21] for more practical applications involving field measurements.

While the above applications use magnetometers in the spin exchange relaxation-free (SERF) regime [22,23], atomic magnetometers also excel at making very sensitive radio-frequency (RF) measurements [24–26] in applications such as nuclear magnetic resonance (NMR) [27–29] and magnetic resonance imaging [30,31]. Below 50 MHz, the fundamental sensitivity of the atomic magnetometer is predicted to be better than conventional coil detection [28]. The magnetometer is easily used with frequencies in the MHz range as only a field of \sim 0.1 mT is needed to set the resonance frequency of the sensor.

In many applications, the magnetometer is shielded from interfering electromagnetic radiation by enclosure in a common conductive layer and is shielded from static magnetic fields by enclosure in a common layer of mu-metal. Measurements are then made by bringing the object to be studied inside the shield. There are, however, applications where the cost of shielding hinders widespread adoption of the magnetic sensing technique or for which shielding is simply not possible. As an example of the latter, a type of zero-field NMR spectroscopy, known as nuclear quadrupole resonance (NQR), can be used to detect landmines buried in the ground [32–35]. Checkpoint applications of NQR, such as for the detection of contraband material or counterfeit pharmaceuticals [36–38], can be done shielded, but would have more widespread adoption if shielding were not required.

Without magnetic shielding, the ambient magnetic field can be compensated for with electromagnetic coils [39,40]. As shown in this work, small additional fluctuations in the ambient magnetic field can be compensated for in real time with a reference signal to continually calibrate the sensors. Without RF shielding, a gradiometer can be used to eliminate interference which is constant over the sensor [41]. With an array of magnetometers [42], more sophisticated schemes can be utilized. With the four-sensor linear array presented here, both constant and linearly varying interference signals are eliminated while the signal from a local source is retained [43]. The signals from the two inner sensors are added and those from the outer sensors are subtracted.

^{*} Corresponding author.

E-mail address: ksauer1@gmu.edu (K.L. Sauer).

Atomic magnetometers are particulary well-suited to forming arrays to be used for interference rejection because they are capable of true independent measurements. Inherently they do not inductively couple to one another, as is the case with conventional coil or RF SQUID detection. They also do not capacitively couple to the environment.

Furthermore, atomic magnetometers also have a high intrinsic dynamic range, only limited on the high end by RF broadening [44]. The high-end limit for the magnetometers used here is on the order of a nT. Therefore, for observing signals on the order of a fT, as for a typical NQR experiment [27], there is the potential for significant rejection of interference by six orders of magnitude.

In our original work [43], using a magnetometer array to detect nuclear quadrupole resonance signals in an unshielded environment, the interference was reduced at most by a factor of 26. Subsequently it was found that the non-linearity of the detected interference was due to the self-resonance of the compensating DC field coils; the self-resonance frequency was in fact close to the interference frequency, 1.31 MHz, from the local radio station. The interference was being re-radiated by the field coils. New field coils were built in which the spacing between the windings was increased to reduce capacitance between them such that the selfresonance was moved away from 1 MHz [45]. The interference rejection was increased, by as much as four times over the original results, but not robustly. Rejection varied by as much as a factor of two from experiment to experiment.

In this work, we show how to make the interference rejection robust. In doing so, the interference was suppressed by as much as a factor of 10 over the original result. In this new approach, a reference signal is now applied concurrently with signal detection. It is phase encoded so that it can be differentiated from the other signals, interference as well as targeted ones, and is used to calibrate the sensor in real time. This real-time calibration depends heavily on the linearity of the receive electronics as well as accurate calibration of the reference signal through electron spin resonance (ESR). A theoretical framework for ESR calibration, taking into account atomic polarization, is presented in Section II and experimentally verified.

2. Theory

The optical signal is the Faraday rotation ϕ of linearly polarized light as it traverses the optically pumped gas of length *l*, transverse to the static field $\mathbf{B}_0 = B_0 \hat{z}$. The frequency v of this probe light is close to that of the D_1 line of ⁸⁷Rb v_1 , but is far enough from this atomic resonance frequency so that the atomic hyperfine splitting, Zeeman shifts, and pressure-broadened optical linewidth are small compared to the off-resonance $|v - v_1|$. In this limit, the optical rotation can be estimated to be [46-48]

$$\phi = \frac{1}{4} I r_e c f N \frac{1}{(\nu - \nu_1)} (\langle \mathbf{F} \cdot \hat{\mathbf{n}} \rangle_2 - \langle \mathbf{F} \cdot \hat{\mathbf{n}} \rangle_1)$$
 (1)

where r_e is the classic electron radius, f is the absorption oscillator strength. N is the atomic number density. \mathbf{F} is the total angular momentum of the atom, and \hat{n} is the direction of propagation of the probe light; to a good approximation this expression is proportional to the electron spin polarization [49]. In the ground state manifold, the hyperfine levels, corresponding to F = 2 and F = 1, are split by the energy $\hbar\omega_{HFS}$; the expectation value of F_n is calculated from the density matrix for each *F*-sublevel ρ_F as follows:

$$\langle F_n \rangle_F = \langle \mathbf{F} \cdot \hat{\mathbf{n}} \rangle_F = \text{Tr}\{\mathbf{F} \cdot \hat{\mathbf{n}} \rho_F, \}.$$
 (2)

where Tr represents the trace operator. The density matrix evolves under the Hamiltonian for the system with an oscillatory piece from the magnetic field \mathbf{B}_1 of frequency ω applied transversely to $\hat{\mathbf{z}}$. The magnetometer is sensitive to fields in the x-y plane. For definiteness $\mathbf{B}_1 = B_1 \cos \omega t \hat{x}$ is taken. The Hamiltonian from the hyperfine and Zeeman interactions can be expressed as the sum of a dominant term H_F and a perturbation term h_F :

$$H_F = a_F + (-1)^F \omega F_z, \tag{3}$$

$$h_F = 2\omega_F F_x \cos \omega t + \left[b_F - (-1)^F \omega\right] F_z + c_F F_z^2, \tag{4}$$

where the Rabi frequency is

$$\omega_F = \frac{g_F \mu_B B_1}{2\hbar}.\tag{5}$$

The other constants in Eqs. (3) and (4), for low magnetic fields,

$$a_F = \frac{\hbar \omega_{HFS}}{8} + (-1)^F \frac{\hbar \omega_{HFS}}{2} \left(1 + \frac{x^2}{2}\right),$$
 (6)

$$b_{F} = \frac{g_{I}\mu_{B}B_{0}}{\hbar} + (-1)^{F} \frac{\omega_{HFS}x}{4}, \tag{7}$$

$$b_{F} = \frac{g_{I}\mu_{B}B_{0}}{\hbar} + (-1)^{F} \frac{\omega_{HFS}x}{4},$$

$$c_{F} = -(-1)^{F} \frac{\omega_{HFS}}{\hbar} \frac{x^{2}}{16},$$
(8)

where the dimensionless parameter x [44] is

$$x = \frac{(g_J - g_I)\mu_B B_0}{\hbar \omega_{\text{MFS}}}. (9)$$

In the interaction representation, the evolution of the density matrix is governed by

$$\hbar \frac{\partial \tilde{\rho_F}}{\partial t} = i \left[\tilde{\rho_F}, \tilde{h}_F \right], \tag{10}$$

where
$$\tilde{\rho}_F(t) \equiv e^{iH_F t/\hbar} \rho_F(t) e^{-iH_F t/\hbar}$$
 (11)

$$\tilde{h}_F \equiv e^{iH_F t/\hbar} h_F e^{-iH_F t/\hbar} \tag{12}$$

$$=(b_F-\omega)F_z+c_FF_z^2$$

$$+2\omega_F(F_x\cos\omega t-(-1)^FF_y\sin\omega t)\cos\omega t.$$
 (13)

Invoking the secular approximation [50], in which the rapidly varying terms are averaged to zero,

$$\tilde{h}_F = (b_F - (-1)^F \omega) F_z + c_F F_z^2 + \omega_F F_x. \tag{14}$$

Since \tilde{h}_F does not depend on time,

$$\tilde{\rho}_{F}(t) = e^{-i\tilde{h}_{F}t/\hbar} \rho_{F}(t=0) e^{i\tilde{h}_{F}t/\hbar}, \tag{15}$$

where

$$\rho_F(t=0) = \frac{e^{F_z \beta}}{\sum_F \sum_{m_F} e^{m_F \beta}},\tag{16}$$

with the spin temperature β corresponding to the spin polarization P [51] as follows:

$$\beta = \ln\left(\frac{1+P}{1-P}\right). \tag{17}$$

The final signal, after a pulse length of t_0 is, from Eq. (1):

$$\phi(t_0) \propto \text{Tr}\Big\{\tilde{\rho}_2 \widetilde{F}_n\Big\} - \text{Tr}\Big\{\tilde{\rho}_1 \widetilde{F}_n\Big\}. \tag{18}$$

If the probe beam is parallel to the excitation direction, along \hat{x} , the final signal is

$$\phi(t_0) \propto \frac{1}{2} [Tr\{\tilde{\rho}_2 F_-\} - Tr\{\tilde{\rho}_1 F_+\}] e^{-i\omega t_0} + c.c.$$
 (19)

or if the probe beam is perpendicular to the excitation direction, along \hat{v} ,

$$\phi(t_0) \propto \frac{i}{2} \left[Tr\{\tilde{\rho}_2 F_-\} + Tr\{\tilde{\rho}_1 F_+\} \right] e^{-i\omega t_0} + c.c. \tag{20} \label{eq:phi0}$$

The key difference between the two orientations of the probe beam is the subtraction of the signal from the different *F* levels, for the parallel case, and the addition for the perpendicular case.

After the termination of the pulse the spins are free to evolve. Ignoring decay for the moment, the signal at time Δt after t_0 would be

$$\begin{split} \phi(t) &\propto \left[\sum_{m} \langle m+1|\tilde{\rho}_{2}(t_{0})|m\rangle \langle m|F_{-}|m+1\rangle e^{i\omega_{m,m+1}^{(2)}\Delta t} \right. \\ &\left. \pm \sum_{m} \langle m|\tilde{\rho}_{1}(t_{0})|m+1\rangle \langle m+1|F_{+}|m\rangle e^{i\omega_{m+1,m}^{(1)}\Delta t} \right] \times e^{-i\omega t}/2 + c.c., \end{split}$$

where

$$\omega_{m\,m+1}^{(2)} = \omega - (E_{m+1} - E_m)/\hbar \quad \text{(for } F = 2\text{)}$$
 (22)

$$\omega_{m+1\,m}^{(1)} = \omega - (E_m - E_{m+1})/\hbar \quad (\text{for } F = 1)$$
 (23)

are the differences between the applied radio-frequency field and the transition frequencies in the Zeeman resonances. The plus sign in Eq. (21) corresponds to the probe beam perpendicular, the minus to the probe beam parallel. The real part of the expression in square brackets in Eq. (21) corresponds to the in-phase part and the imaginary to the out-of-phase part in the resulting spectra.

For the calibration of the reference signal, the strength of the excitation field is varied for a given pulse length t_p and the resulting signal is fit to a sinusoid. For delta-function pulses [52], in which no hyperfine evolution occurs, the resulting signal would give an exact calibration with a null signal or zero-crossing corresponding to the tip angle $\theta \equiv \mu_B B_1 t_p / h = \pi$. The zero crossing can be used as a metric of the accuracy of the fit. For 100% polarization the F=1 sub-level is unpopulated and with a finite pulse the zero-crossing would be close to $\theta=\pi$. Deviations from the ideal case become pronounced with lower polarizations and finite pulses.

Predictions for positive polarization, the end-state $|F,m_F\rangle=|2,2\rangle$ is most highly populated, and for negative polarization, whereby the end-state $|2,-2\rangle$ is most highly populated, are shown in Fig. 1 for a B_0 field of 0.19 mT. For positive polarization, the frequency of excitation is matched to the $|2,1\rangle \rightarrow |2,2\rangle$ transition. All other transition levels, both in the F=2 multiplet and in

the F=1 multiplet, are higher in frequency, as shown in Fig. 2. For the negative polarization, the frequency of excitation is matched to the $|2,-1\rangle \rightarrow |2,-2\rangle$ transition; in this case, all other transition frequencies in the F=2 multiplet are lower than the excitation frequency and the F=1 multiplet transition frequencies are higher in frequency.

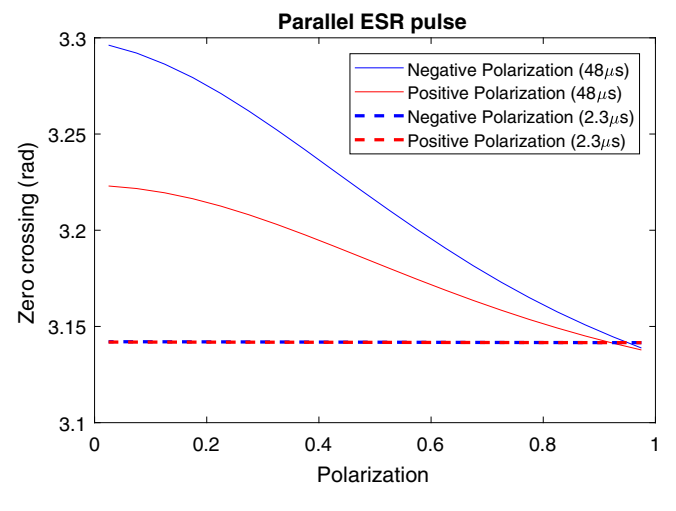
In all cases, as expected, the short pulses show no dependency on polarization. For the longer pulses, the positive polarization has less variation as a function of frequency. In particular, for the case where the probe beam is perpendicular to the RF excitation, the off-resonance effects of the two multiplets tend to compensate for one another, and the variation is less than 0.5%. Therefore, if the system is limited in power such that longer, weaker pulses are unavoidable, a more accurate calibration of the reference pulses would be achieved if the polarization of the sensor were positive and the excitation were orthogonal to both the pump and probe beams.

3. Experimental design

The experimental setup is similar to that of previous experiments [45,43] but with some important improvements, as discussed in detail in this section. As shown in Fig. 3, an array of four optically pumped atomic magnetometers from Twinleaf [53] with a baseline of 25 cm are placed inside a set of three pairs of compact coils used to compensate for Earth's fields as well as to set the magnetometer's resonance frequency to the frequency of interest.

3.1. Sensor readout

The vapor cell of the magnetometer consists of isotopically enriched 87 Rb with 0.8 amg of Neon as a buffer gas, 0.05–0.06 amg of N₂ as a quenching gas [54,55], and has an effective volume of 0.36 cm³. The cell is heated to 140 °C and pumped at the D₁ resonance for 87 Rb using circularly polarized light; the input to the pump fiber was 200 mW for each sensor. The linearly polarized probe is orthogonal to the pump and is about 0.12 nm off of the D₁ line. The linearly polarized probe passes through the vapor twice and experiences a small rotation, ϕ of Eq. (1), in polarization which is measured by a balanced polarimeter [56]. In the case of a small steady-state signal, the transverse value of F is proportional to the magnetic field \mathbf{B}_1 [24].



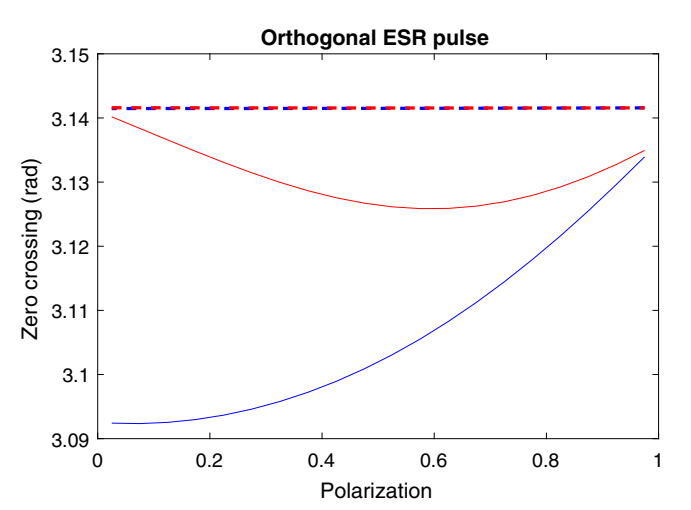


Fig. 1. The tip angle, θ , at which the signal goes to zero, is used as a metric of the calibration. The ESR pulse can be applied in a direction that is either parallel (left) or orthogonal (right) to the probe beam. This direction, along with the polarization and pulse direction, will affect the calibration. By comparing the scales on the graphs it is clear that for the 48 μs pulse (solid lines) the orthogonal pulse varies much less than the parallel pulse over the polarization range. The 2.3 μs pulses are effectively equivalent in all cases (dashed lines).

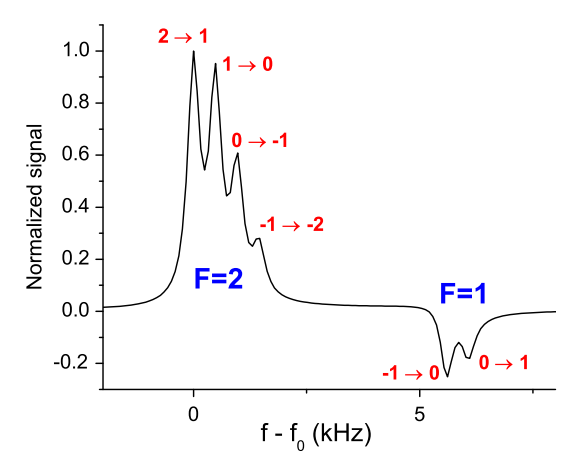


Fig. 2. An example spectrum is given by $t_P=2.3~\mu s$, $\theta=18^\circ$ pulse at 20% polarization with $B_0=0.19~mT$. Each peak is labeled by F level (blue) and m_F sublevel (red). (For interpretation of the references to colour in this figure legend, the reader is referred to the web version of this article.)

A TecMag spectrometer [57] was used to measure the electronic signal produced from the balanced polarimeter. The spectrometer was found to have a non-linear response to voltage inputs, Fig. 4, which hindered the efficiency of the suppression algorithm for

signals of varying sizes. To take advantage of the dynamic range spanning four orders of magnitude, an external pre-amplifier was used. With this configuration, only 0.5% residual from a linear fit was found, an order of magnitude improvement. This improvement is shown in black in the inset of Fig. 4. Likewise, the phase of the signal varied greatly using the internal amplifiers. Using the external amplifiers, however, reduced this effect significantly. The 0.5% residual was key to obtaining rejection factors of around 200.

3.2. Fields

To study interference rejection, the magnetometers are tuned to the frequency of a local radio station at 1.31 MHz. Field coils, common to all four sensors, are used to compensate for Earth's field and to set the magnetometer's resonance frequency. In addition, each sensor has individual coils to provide more localized field control. To avoid re-radiation of the interference from the field coils and its non-linear contribution to the local field [43], coils with a smaller footprint and fewer turns are used [45]. Wider spacing between coils reduces capacitance between windings. Consequently, the self-resonance is shifted away from 1.31 MHz. Additionally, adding ferrite rings to the static field coils helped to choke-out any RF signal picked up by the coils.

In addition to the local re-radiation of interference, the AC line present in the building was also observed to shift the resonance

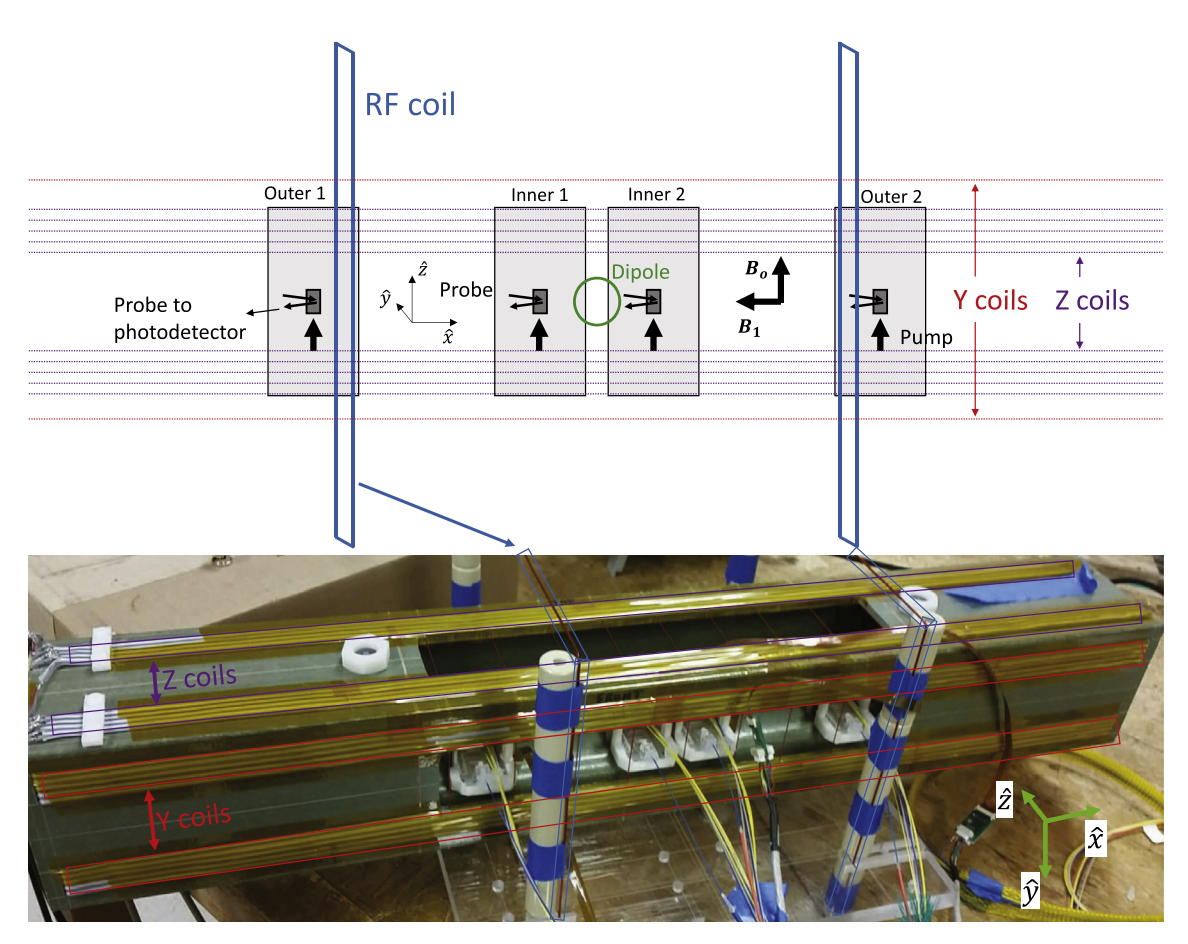


Fig. 3. The array of four magnetometers is centered in the fiberglass-reinforced polyester (FRP) frame. A schematic is shown on top, and the corresponding photo on the bottom (minus the small coil used as a magnetic dipole source). The ribbon wire is wrapped symmetrically around the array and used to control local static fields. The RF fields used for reference signals are generated by the large square coils attached to the ceramic posts with blue tape. The pump and probe beams are fiber-coupled into the cell. A third laser beam is fiber-coupled with the fiber end embedded in a ceramic heating element placed near the cell; the power of the laser is used to control the temperature of the oven. From left to right, the sensors will be referred to as Outer 2, Inner 1, Inner 2, and Outer 1. (For interpretation of the references to colour in this figure legend, the reader is referred to the web version of this article.)

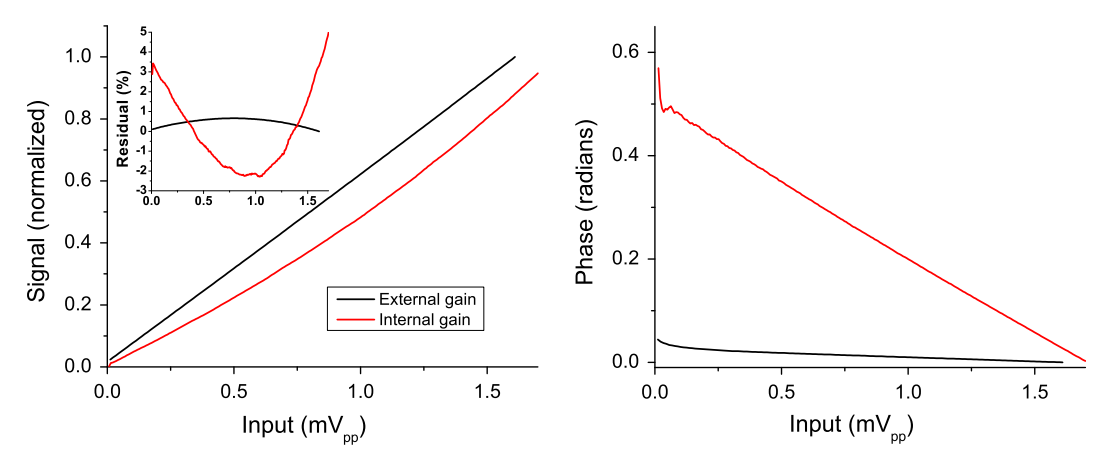


Fig. 4. The spectrometer was found to have a non-linear response in signal (left) and phase (right) at certain gain settings (red) so a fixed gain setting was used and additional amplification was provided by external pre-amplifiers (black). (For interpretation of the references to colour in this figure legend, the reader is referred to the web version of this article.)

frequency of the sensors. Therefore, all of equipment was put on an AC power conditioner and sequences were triggered off of the AC line. Furthermore, the ferrite rings placed on the field coils greatly reduced the 60 Hz footprint that was present in previous work [43].

A small loop of current with radius R=1 cm, pointing in the \hat{y} direction, was used to simulate a near-field signal of interest. A two-dimensional vector measurement can be made by considering the phase of the signal in the two directions orthogonal to the pump direction [58]. The field **B** from the loop can be approximated as a magnetic dipole with magnetic moment $\mathbf{m} = m\hat{y}$,

$$\mathbf{B}(\mathbf{r}) \approx \frac{\mu_0}{4\pi r^3} [3(\mathbf{m} \cdot \hat{r})\hat{r} - \mathbf{m}], \tag{24}$$

where ${\bf r}$ is the displacement from the loop. At the magic angle [52], $\hat{y} \cdot \hat{r} = 1/\sqrt{3}$, the B_y field changes sign. This is useful in an array as it specifies the distance the outer sensor must be from the dipole in order to have all signals generated by the dipole add under the interference rejection algorithm. A 2D vector measurement can be made by decomposing the acquired signal into its real and imaginary components and using the reference signal to phase it appropriately. Displayed in Fig. 5 is a model of the signal from a dipole overlaid with vector-resolved measurements for each of the four sensors.

3.3. Phase cycling and 2D spectroscopy

As in a spin-lock spin-echo pulse sequence [59-61], the data is acquired in N separate, but consecutive, windows. Normally, a refocusing pulse is inserted between the windows, followed by some dead time. It is during this time that the atoms are pumped. Details of the sequence are shown in Fig. 6.

During the windows, data from the ambient signal and the reference signal is acquired. The reference signal, however, is phase-alternated, changing by π with each new window. To observe the ambient signal, consecutive windows are added, removing the reference signal and leaving N/2 data sets. To observe the reference signal, consecutive windows are subtracted. Any field shifts can be easily be seen by changes in the magnitude and phase of the reference signal. Figure 7 shows how the reference signal (\sim 20 pT) closely matches the interference signal of roughly the same size. Therefore, corrections to the ambient signal, including both interference and signals of interest, can be done in real time.

Once the ambient signal is calibrated via the reference signal, the data is Fourier transformed. The on-resonance peaks of this spectrum are Fourier transformed a second time. This gives a 2D spectrum which has \sim 1 Hz resolution, with the signal of interest, as from the current loop, placed on resonance. Finally, the rejection algorithm consists of adding signals from the inner two sensors and subtracting those from the outer two sensors to gain the final sensitivity values of 15 fT/ $\sqrt{\rm Hz}$.

4. Results and discussion

4.1. Calibrating the reference signal

In previous works, calibration of the magnetometers yielded results which were not robust over time [43,45]. Fig. 6 shows the ESR pulse sequence and Fig. 8 shows typical calibration curves for $t_p=48~\mu s$ excitation pulses. However, the calibration for this length of pulse has a polarization dependence, as shown in Fig. 9, leading to an unreliable calibration. Also shown in Fig. 9, a shorter pulse of 2.3 μs provides a more robust experiment, as predicted in Section 2. For the shorter, stronger pulse, the voltage into the coil that produced the reference signal is quite large, twenty times higher than the voltages used for the longer, weaker pulses. Therefore the signal from a small coil is used as a measure of the field, in particular, the net area under the pulse, which includes $\sim 0.5~\mu s$ rise and fall times.

For all calibrations, the cell temperature is decreased to $100\,^{\circ}$ C. There are two reasons to reduce the temperature. The first reason is to reduce the decay of transverse polarization during the excitation pulse down to the limit dictated by the field inhomogeneity, around a ms, so as to keep the calibration uncorrupted. In the limit of low polarization, and therefore faster decay [62], the intrinsic relaxation rate is directly proportional to the Rb number density which is increased with temperature. The second reason is to ensure that the Faraday rotation of the probe light stays within the small angle approximation, so that the response of the balanced polarimeter [56] stays within a linear regime [43]. At $100\,^{\circ}$ C, the maximum Faraday rotation for the optimal tip angle, $\theta = \pi/2$, and 100% polarization is 0.2 rad.

In Section 2, the response to an RF pulse was modeled over a range of polarizations, including both positive and negative values, and two different pulse times. As shown in Fig. 10, at longer pulse lengths the zero-crossing of a π pulse deviates significantly (3–5%) at low polarization as predicted. This corresponds to an increased pulse field needed for a full π rotation, as seen in Fig. 9, and deviations from a pure sinusoid, as seen in Fig. 8.

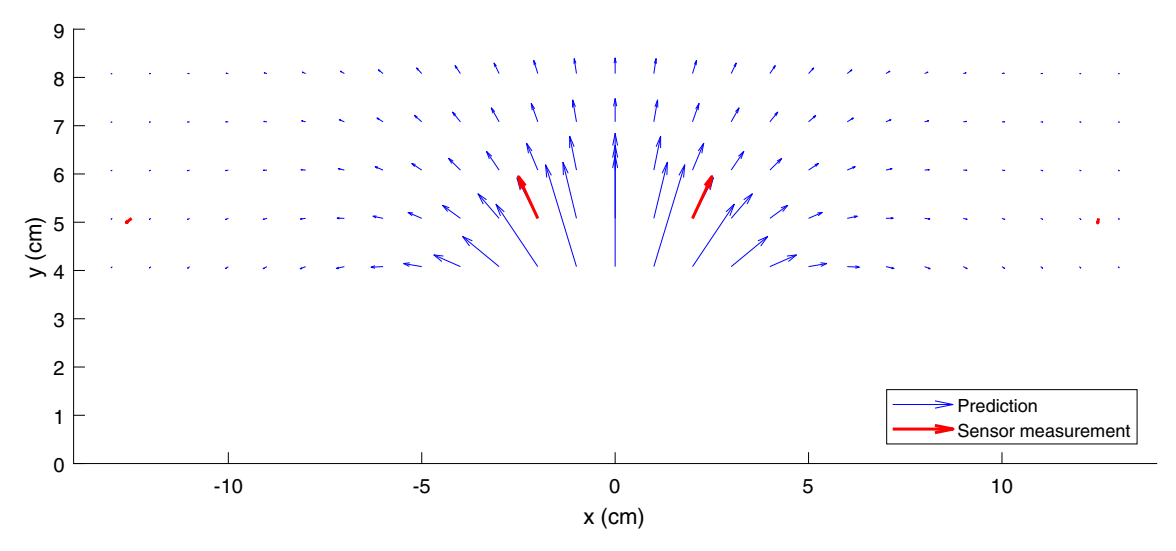


Fig. 5. A near-field signal of interest was generated from a small current loop placed at the origin. The data was calibrated to the reference signal to make the \hat{y} direction correspond to the real part of the signal and the \hat{x} direction to the imaginary part.

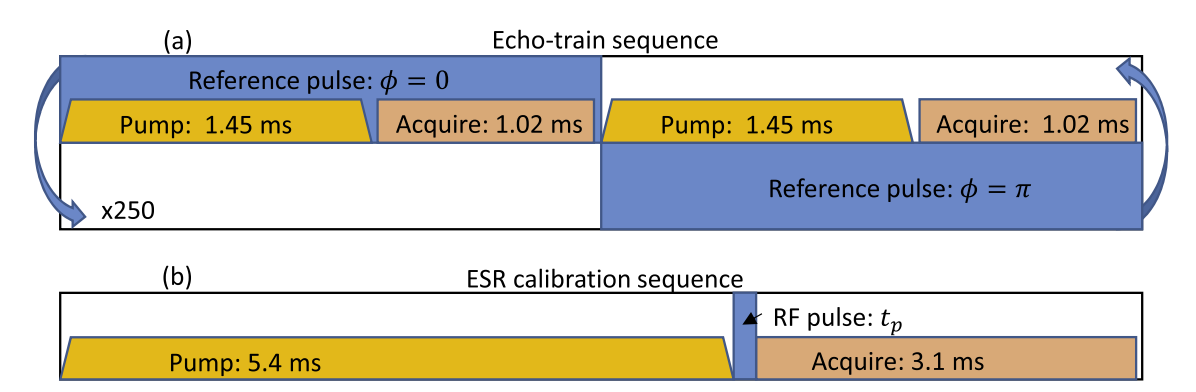


Fig. 6. (a) A reference field is applied during both optical pumping and data acquisition, but changes phase by π every other repeat unit; the total number of repeat units is 500 and the timing mimics what would be used in a spin-echo train. (b) The ESR sequence is used to calibrate the reference field; a strong RF pulse of duration t_p and varying magnitude induces a free induction decay during the acquire window.

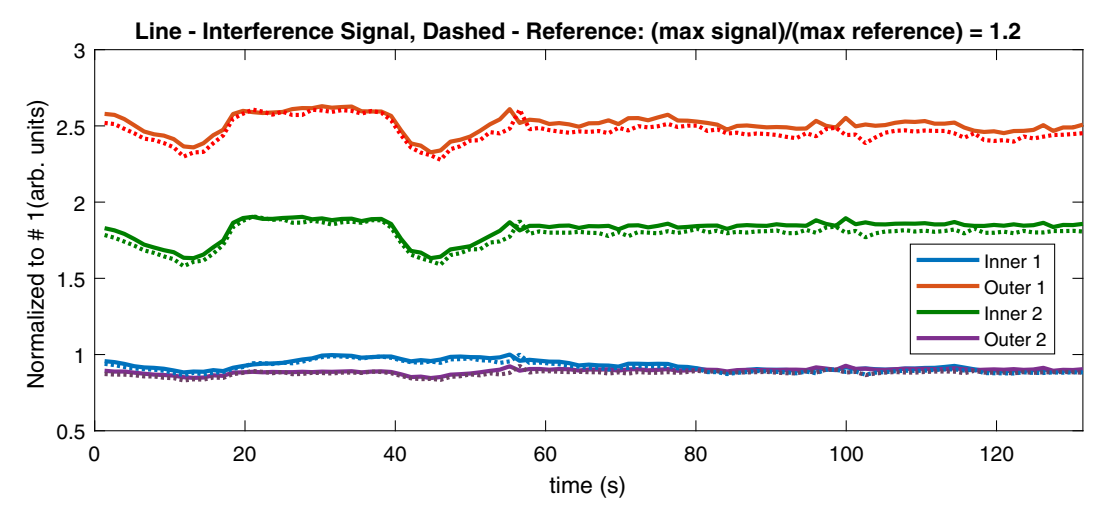


Fig. 7. As observed in the figure, shifts in the resonance frequency of the atoms cause the signal, both reference (dashed line) and interference (solid), to change over time. The reference signal, applied in real time, can correct for such changes. In the above, the data has been normalized to the maximum value of Inner Sensor 1.

After the RF pulse is over, the m_F level populations are calculated at various polarization and tip angles and compared to experimental data, Fig. 11. This gives insight into the spin dynamics

driving the calibration deviations. In the prediction, a transverse (or spin-spin) relaxation time T_2 of approximately 1 ms is used in the prediction. As expected for the short pulse, a shift from the

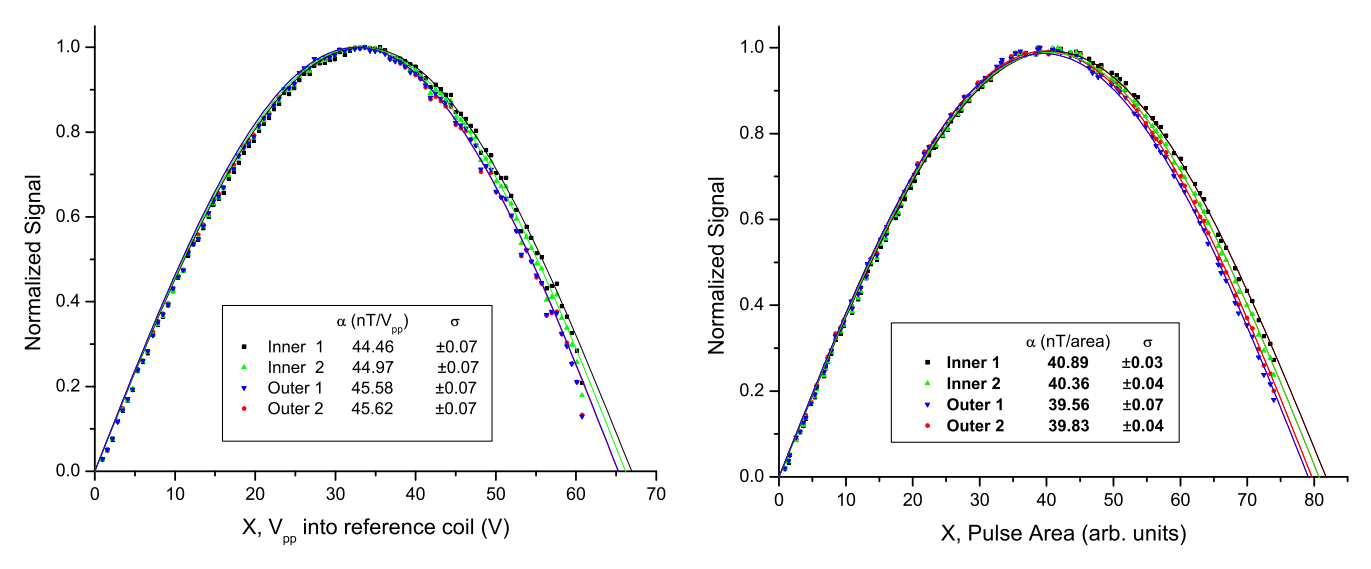


Fig. 8. For a fixed pulse length, 48 μs (left) and 2.3 μs (right), the excitation field is varied. For the longer, weaker pulses, the voltage into the reference coil is used as a metric of the field; for the shorter, stronger pulses, the net signal from a small nearby coil is used. By fitting the response to a sinusoid, $\sin(\frac{\pi}{2}\frac{\chi}{\chi_o})$, a calibration factor, $\alpha = 1/(2X_o\gamma t_p)$ is obtained, where $\gamma = 7$ MHz/mT.

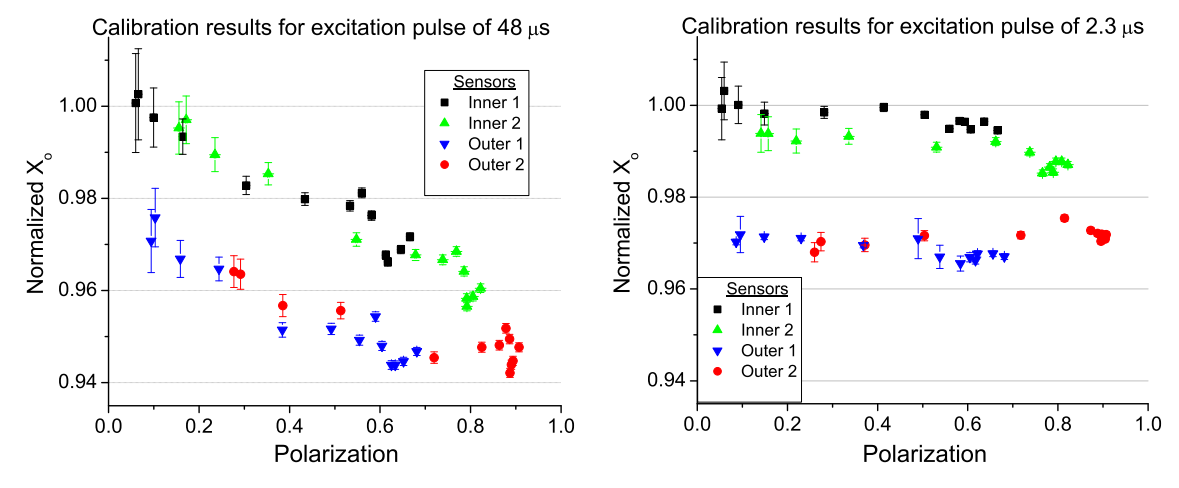


Fig. 9. When a long pulse (left) is applied to the system, a change in calibration factor X_o , Fig. 8, is observed based on the atomic polarization while the short pulse (right) has little dependence on polarization.

higher m_F states to the lower m_F states is seen as the tip angle is increased towards π . This behavior is also seen for the longer pulse, but only at short tip angles. Closer to π , the off-resonant effects introduced by the non-linear Zeeman splittings become apparent, particularly for the low polarization case where the F=1 sublevel has a significant population.

Accurate measurement and analysis of the ESR calibration data is pivotal to the success of the rejection algorithm. The rejection algorithm uses the relative signal sizes, as calibrated by the reference signal, of each sensor to perform noise cancellation. Put simply, the more accurate the relative signal sizes are measured, the more accurate the noise cancellation will be.

4.2. Radio-frequency interference mitigation

Previously, the orientation of the array has been observed to significantly affect the degree of rejection of interference, by as much as a factor of 6 [43]. For this reason data was taken in multiple orientations denoted by the orientation with respect to a nearby wall, the parallel (\parallel) and perpendicular (\perp) directions, and a direction, approximately 45° between the two. Over the

course of a week, the array was cycled through the various orientations. With each new orientation, a calibration of the reference signal was done with both a long and a short excitation pulse. With the 2.3 μ s excitation pulse, the calibration factor α changed by less than 0.25% for each sensor, with the 48 μ s excitation pulse variations were as high as 1.5%. This shows the robustness of using the shorter pulses and bodes well for doing the calibration of the reference signal only when the resonance frequency is changed.

To separate out the interference rejection from the intrinsic sensitivity of the array, the magnetometer is operated at two resonance frequencies, one at 1.31 MHz, the nominal frequency of a local radio station, and one at 1.28 MHz, outside the bandwidth of the radio station. Data is shown in Fig. 12, both for a single sensor in (a), and for the whole array in (b) and (c). The large peak shown in Fig. 12(a) is caused by the radio station signal and it is about a Hz away from the resonance frequency of 1.31 MHz. By using the array, Fig. 12(b), the interference signal is reduced by a factor of 120. Note the change of scale from Fig. 12(a) and (b). In other orientations, the interference is suppressed by factors up to 250. This represents an improvement in the rejection by more than a factor of 2 over previous results [45].

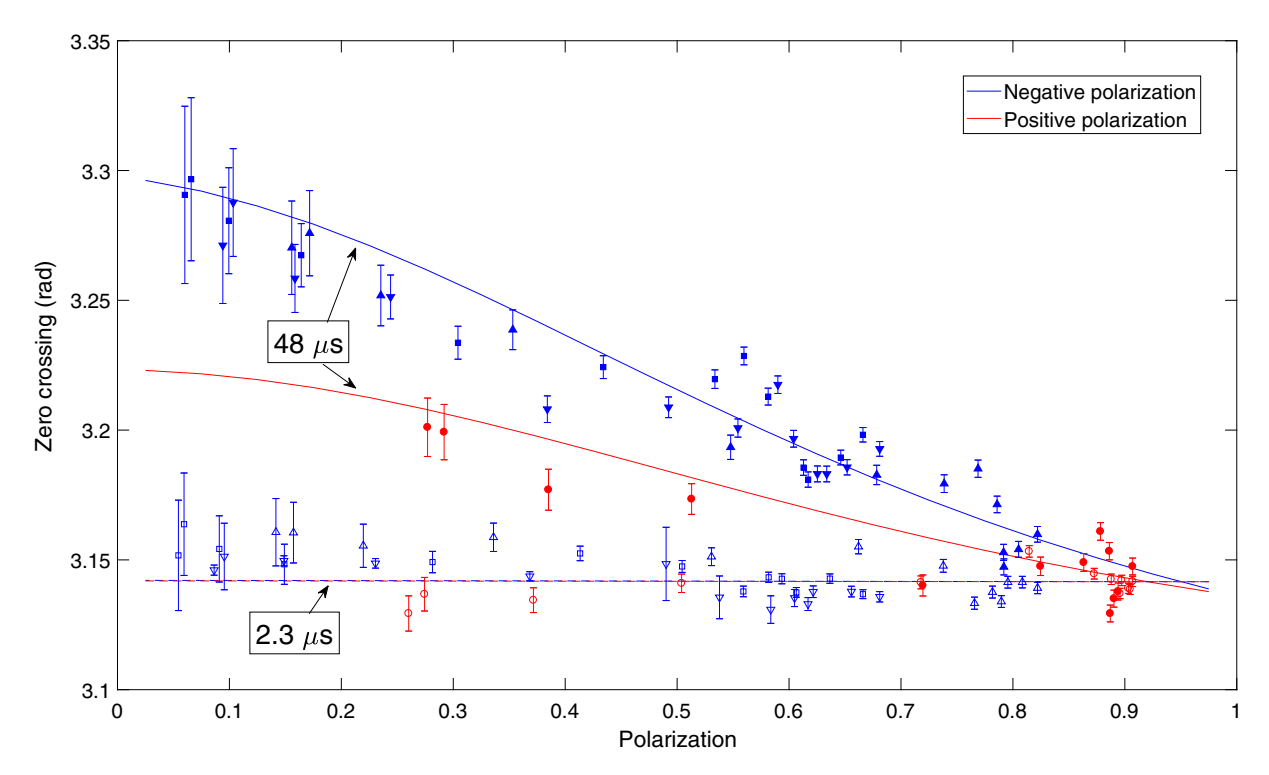


Fig. 10. The model (lines) derived from a density matrix formulation predicts significant deviations in the spin evolution for various polarizations and long, 48 μs, pulse lengths. Negative polarization (blue) shows a higher deviation than positive polarization (red). Sensor data is overlayed with a universal scaling factor to align high polarization data with π . The symbol shapes correspond to the same symbols as used in Fig. 9. (For interpretation of the references to colour in this figure legend, the reader is referred to the web version of this article.)

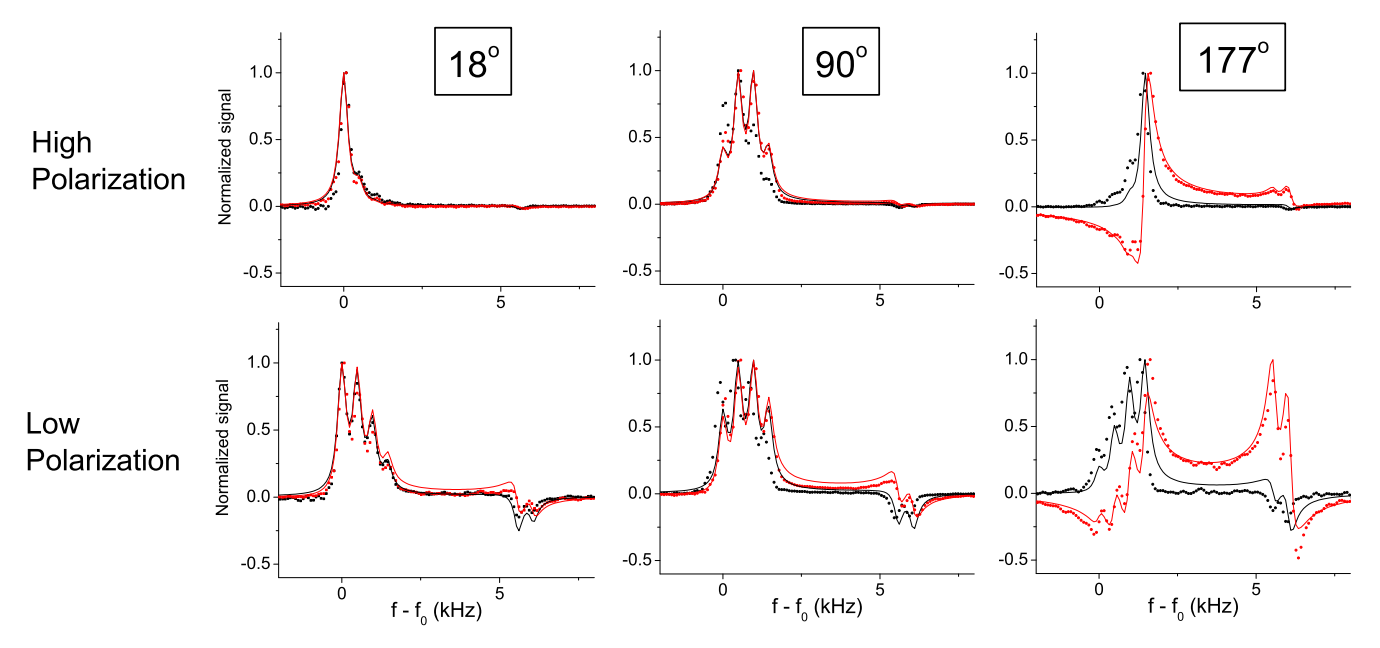


Fig. 11. The spectra from outer sensor 2, which has positive polarization, is shown above for various tip angles θ . The black and red lines show the modeled transition probabilities for each case with a 2.3 μs (black) and 48 μs (red) pulse. The individual m_F transitions are labeled in Fig. 2. (For interpretation of the references to colour in this figure legend, the reader is referred to the web version of this article.)

Further, to demonstrate the ability to retain a weak signal from a local source, data is also taken with a small oscillating dipole, created by a current loop as shown in Fig. 12(a) and (c). This dipole source is strongly detected on the inner sensors, with field strengths of \sim 100 fT, but not on the outer sensors, as near field radiation falls off as $1/r^3$, Eq. (24). To distinguish this coherent signal from noise, both the standard deviation around the mean σ and

the root-mean-square (RMS) values are calculated from 100 scans; the former is the incoherent noise, the latter includes coherent signals. For a single sensor the dipole signal is clear when its frequency is well away from that of the radio station, Fig. 12(a), but is obscured when its frequency is close to that of the radio station. When using the signal from the full array, however, the dipole signal is revealed, Fig. 12(c). Note, it appears there is some corruption

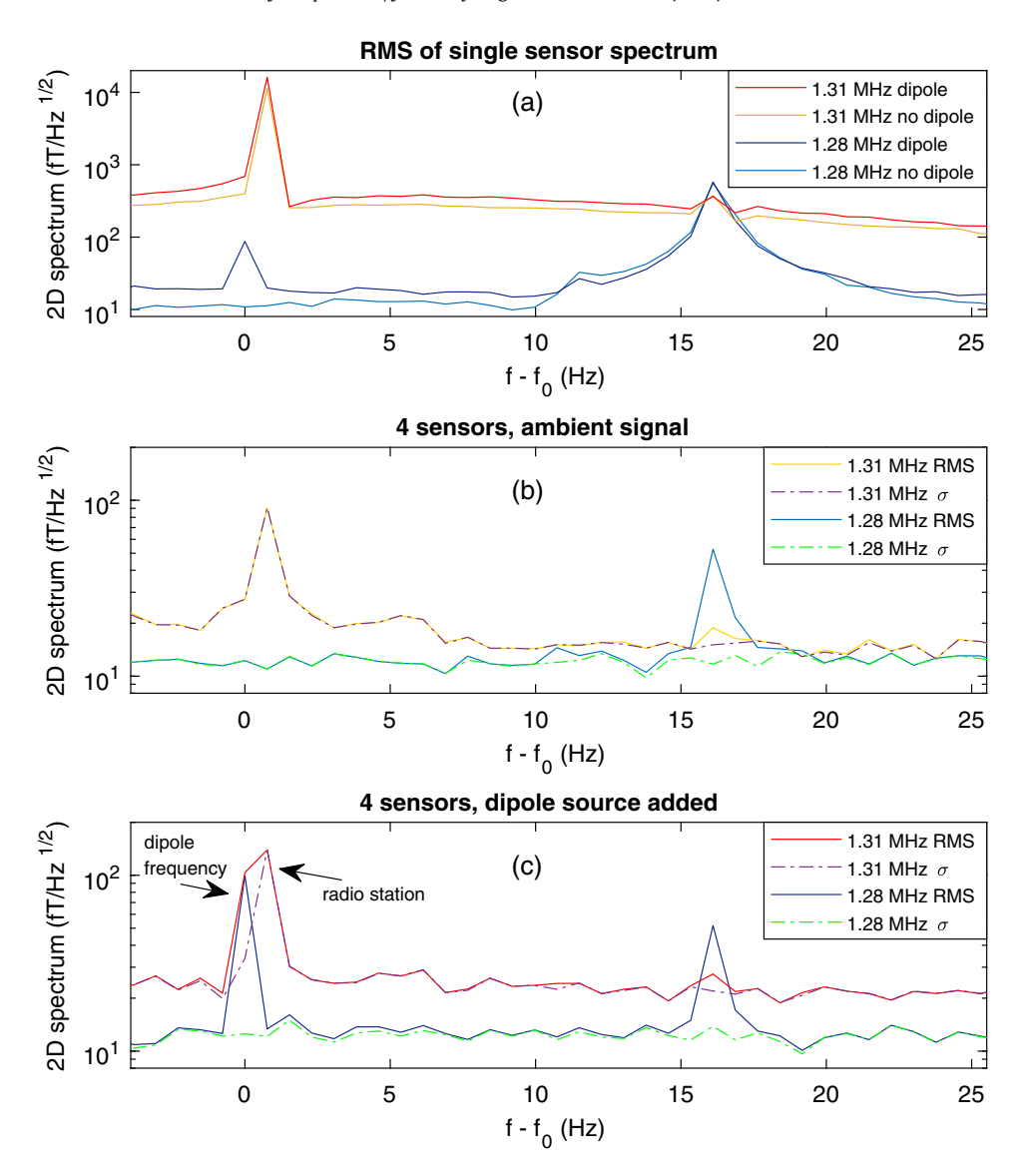


Fig. 12. Graph (a) displays the root-mean-square (RMS) of the spectra for a single inner sensor at a frequency near the radio noise (yellow) and 30 kHz away from it (light blue). The signal from a small oscillating dipole is obscured in the former case (red) and clear in the latter case (dark blue). The bottom two graphs are the result of applying the rejection algorithm to the data from all four of the sensors without (b) and with (c) the dipole source. The radio noise, seen 1 Hz away from the dipole signal, is still present, but reduced by a factor of 120 from the top graph. The standard deviation σ shows incoherent noise while the RMS includes coherent sources, as from the dipole whose signal is now clearly visible in (c). (For interpretation of the references to colour in this figure legend, the reader is referred to the web version of this article.)

in the cancellation in Fig. 12(c), due to re-radiation of the interference from the dipole. There is no such corruption without the dipole, Fig. 12(b), and the spectra at the two frequencies converge quickly off-resonance.

The radio station is representative of a far-off source of interference, which would be expected to have a close-to-linear spatial variation over the sensor array. The unshielded array sits, however, in the middle of a noisy laboratory environment, including noise from the instrumentation associated with the operation of the array. This noise would have more deviation from linear than a far-off source [45] and could very well be coherent with the spectrometer. An example of such noise is seen by the 16 Hz noise peak in the 1.28 MHz spectra. By using the full array, this interference is reduced by a factor of 10 over a single sensor. As can be seen in Fig. 12(b), the RMS value is much larger that the σ value; although not shown, this is also the case for the individual sensors. This is indicative that this noise is coherent with, and therefore ultimately results from, the spectrometer. No effort was made to isolate this source of noise; this will be explored in future work.

5. Conclusions

By creating field coils that do not self-resonate near the frequency of interest, choking out additional noise picked up by them, as well as ensuring that signal measured by the spectrometer increased linearly with voltage, sensitivity and rejection has greatly improved from previous experiments. Furthermore, properly calibrating the magnetometers with short ESR pulses gave precise relative signal ratios which greatly contributed to the overall interference rejection ratio. The model predicts that an ESR pulse orthogonal to the pump and probe directions produces a higher stability atomic response and will be explored experimentally in future research. Using real-time reference signals to calibrate the fields has enabled more accurate field corrections that further increase interference rejection. 2D spectroscopy was used to gain a 0.8 Hz resolution, which allows clear identification of offresonance noise. It has been shown that an array of optically pumped magnetometers can achieve sensitivities on the order of 15 fT/ $\sqrt{\text{Hz}}$ with a factor of 100–250 interference rejection. This

allows for an effective method of detecting localized signal sources in the midst of large far-field interference. The methods employed in this setup enable a robust method of unshielded detection of fT signals and interference suppression.

Acknowledgements

This work was supported by the National Science Foundation (award #1711118) as well as the US Army: Night Vision and Electronic Sensors Directorate (MTEQ: #W909MY-12-D0008/0024). R. C. would also like to acknowledge support from the George Mason University Presidential Fellowship and the Mason College of Science Dean's Award.

References

- [1] J. Belfi, G. Bevilacqua, V. Biancalana, S. Cartaleva, Y. Dancheva, L. Moi, Cesium coherent population trapping magnetometer for cardiosignal detection in an unshielded environment, J. Opt. Soc. Am. B 24 (2007) 2357–2362.
- [2] G. Bison, N. Castagna, A. Hofer, P. Knowles, J.-L. Schenker, M. Kasprzak, H. Saudan, A. Weis, A room temperature 19-channel magnetic field mapping device for cardiac signals, Appl. Phys. Lett. 95 (2009) 173701, https://doi.org/10.1063/1.3255041.
- [3] C. Johnson, P.D.D. Schwindt, M. Weisend, Magnetoencephalography with a two-color pump-probe, fiber-coupled atomic magnetometer, Appl. Phys. Lett. 97 (2010) 243703, https://doi.org/10.1063/1.3522648.
- [4] K. Kamada, Y. Ito, T. Kobayashi, Human MCG measurements with a high-sensitivity potassium atomic magnetometer, Physiol. Meas. 33 (2012) 1063.
- [5] K. Kim, S. Begus, H. Xia, S.-K. Lee, V. Jazbinsek, Z. Trontelj, M.V. Romalis, Multichannel atomic magnetometer for magnetoencephalography: a configuration study, NeuroImage 89 (2014) 143–151.
- [6] O. Alem, T.H. Sander, R. Mhaskar, J. LeBlanc, H. Eswaran, U. Steinhoff, Y. Okada, J. Kitching, L. Trahms, S. Knappe, Fetal magnetocardiography measurements with an array of microfabricated optically pumped magnetometers, Phys. Med. Biol. 60 (2015) 4797.
- [7] A.P. Colombo, T.R. Carter, A. Borna, Y.-Y. Jau, C.N. Johnson, A.L. Dagel, P.D.D. Schwindt, Four-channel optically pumped atomic magnetometer for magnetoencephalography, Opt. Express 24 (2016) 15403–15416.
- [8] M.N. Livanov, AN. Koslov, S.E. Sinelnikova, J.A. Kholodov, V.P. Markin, A. Gorbach, AV. Korinewsky, Record of the human magnetocardiogram by the quantum gradiometer with optical pumping, Adv. Cardiol. 28 (1981) 78–80.
- [9] R. Wyllie, M. Kauer, G.S. Smetana, R.T. Wakai, T.G. Walker, Magnetocardiography with a modular spin-exchange relaxation-free atomic magnetometer array, Phys. Med. Biol. 57 (2012) 2619.
- [10] S. Morales, M.C. Corsi, W. Fourcault, F. Bertrand, G. Cauffet, C. Gobbo, F. Alcouffe, F. Lenouvel, M.L. Prado, F. Berger, G. Vanzetto, E. Labyt, Magnetocardiography measurements with ⁴He vector optically pumped magnetometers at room temperature, Phys. Med. Biol. 62 (2017) 7267.
- [11] H. Xia, A. Ben-Amar Baranga, D. Hoffman, M.V. Romalis, Magnetoencephalography with an atomic magnetometer, Appl. Phys. Lett. 89 (2006) 211104, https://doi.org/10.1063/1.2392722.
- [12] E. Boto, S.S. Meyer, V. Shah, O. Alem, S. Knappe, P. Kruger, T.M. Fromhold, M. Lim, P.M. Glover, P.G. Morris, R. Bowtell, G.R. Barnes, M.J. Brookes, A new generation of magnetoencephalography: room temperature measurements using optically-pumped magnetometers, NeuroImage 149 (2017) 404–414.
- [13] H.B. Dang, A.C. Maloof, M.V. Romalis, Ultrahigh sensitivity magnetic field and magnetization measurements with an atomic magnetometer, Appl. Phys. Lett. 97 (2010) 151110, https://doi.org/10.1063/1.3491215.
- [14] M.J. Usher, W.F. Stuart, S.H. Hall, A self-oscillating rubidium vapour magnetometer for geomagnetic measurements, J. Sci. Instrum. 41 (1964) 544.
- [15] S. Pustelny, D.F. Jackson Kimball, C. Pankow, M.P. Ledbetter, P. Wlodarczyk, P. Wcislo, M. Pospelov, J.R. Smith, J. Read, W. Gawlik, D. Budker, The global network of optical magnetometers for exotic physics (gnome): a novel scheme to search for physics beyond the standard model, Annalen der Physik 525 (2013) 659–670. https://onlinelibrary.wiley.com/doi/pdf/10.1002/andp.201300061>.
- [16] P. Wodarczyk, S. Pustelny, D. Budker, M. Lipiski, Multi-channel data acquisition system with absolute time synchronization, Nucl. Instrum. Methods Phys. Res., Sect. A 763 (2014) 150–154.
- [17] J. Lee, A. Almasi, M. Romalis, Improved limits on spin-mass interactions, Phys. Rev. Lett. 120 (2018) 161801.
- [18] S.N. Ern, H.D. Hahlbohm, H. Lbbig, Theory of rf-biased superconducting quantum interference device for nonhysteretic regime, J. Appl. Phys. 47 (1976) 5440–5442, https://doi.org/10.1063/1.322574.
- [19] M. Schmelz, V. Zakosarenko, A. Chwala, T. Schönau, R. Stolz, S. Anders, S. Linzen, H.-G. Meyer, Thin-film-based ultralow noise SQUID magnetometer, IEEE Trans. Appl. Supercond. 26 (2016) 1–5.
- [20] L. Lu, J. Shang, Z. Pan, Y. Ji, Chip-scale serf atomic magnetometer without magnetic shield, in: 2017 IEEE 67th Electronic Components and Technology Conference (ECTC), 2017, pp. 1900–1905.

- [21] O. Alem, R. Mhaskar, R. Jiménez-Martínez, D. Sheng, J. LeBlanc, L. Trahms, T. Sander, J. Kitching, S. Knappe, Magnetic field imaging with microfabricated optically-pumped magnetometers, Opt. Express 25 (2017) 7849–7858.
- [22] J.C. Allred, R.N. Lyman, T.W. Kornack, M.V. Romalis, High-sensitivity atomic magnetometer unaffected by spin-exchange relaxation, Phys. Rev. Lett. 89 (2002) 130801.
- [23] I.M. Savukov, M.V. Romalis, Effects of spin-exchange collisions in a high-density alkali-metal vapor in low magnetic fields, Phys. Rev. A 71 (2005) 023405
- [24] I.M. Savukov, S.J. Seltzer, M.V. Romalis, K.L. Sauer, Tunable atomic magnetometer for detection of radio-frequency magnetic fields, Phys. Rev. Lett. 95 (2005) 063004.
- [25] I. Savukov, T. Karaulanov, M.G. Boshier, Ultra-sensitive high-density Rb-87 radio-frequency magnetometer, Appl. Phys. Lett. 104 (2014) 023504, https://doi.org/10.1063/1.4861657.
- [26] W. Chalupczak, R.M. Godun, S. Pustelny, Radio-frequency spectroscopy as a tool for studying coherent spin dynamics and for application to radiofrequency magnetometry, Adv. Atomic Mol. Opt. Phys. (2018), https://doi. org/10.1016/bs.aamop.2018.03.001.
- [27] S.-K. Lee, K.L. Sauer, S.J. Seltzer, O. Alem, M.V. Romalis, Subfemtotesla radio-frequency atomic magnetometer for detection of nuclear quadrupole resonance, Appl. Phys. Lett. 89 (2006) 214106.
- [28] I.M. Savukov, S.J. Seltzer, M.V. Romalis, Detection of NMR signals with a radio-frequency atomic magnetometer, J. Magn. Reson. 185 (2007) 214–220.
- [29] G. Liu, X. Li, X. Sun, J. Feng, C. Ye, X. Zhou, Ultralow field NMR spectrometer with an atomic magnetometer near room temperature, J. Magn. Reson. 237 (2013) 158–163.
- [30] I.M. Savukov, V.S. Zotev, P.L. Volegov, M.A. Espy, A.N. Matlashov, J.J. Gomez, R. H. Kraus Jr., MRI with an atomic magnetometer suitable for practical imaging applications, J. Magn. Reson. 199 (2009) 188–191.
- [31] I. Savukov, T. Karaulanov, Anatomical MRI with an atomic magnetometer, J. Magn. Reson. 231 (2013) 39–45.
- [32] A.D. Hibbs, G.A. Barrall, P.V. Czipott, D.K. Lathrop, Y.K. Lee, E.E. Magnuson, R. Matthews, S.A. Vierkoetter, Land mine detection by nuclear quadrupole resonance, Proc. SPIE (1998) 522–532.
- [33] A.N. Garroway, M.L. Buess, J.B. Miller, B.H. Suits, A.D. Hibbs, G.A. Barrall, R. Matthews, L.J. Burnett, Remote sensing by nuclear quadrupole resonance, IEEE Trans. Geosci. Remote Sens. 39 (2001) 1108–1118.
- [34] J.B. Miller, G.A. Barrall, Explosives detection with nuclear quadrupole resonance: an emerging technology will help to uncover land mines and terrorist bombs, Am. Sci. 93 (2005) 50–57.
- [35] M. Ostafin, B. Nogaj, ¹⁴N-NQR based device for detection of explosives in landmines, Measurement 40 (2007) 43–54.
- [36] J. Shinohara, H. Sato-Akaba, H. Itozaki, Nuclear quadrupole resonance of methamphetamine hydrochloride, Solid State Nucl. Magn. Resonance 43–44 (2012) 27–31.
- [37] J. Barras, K. Althoefer, M.D. Rowe, I.J. Poplett, J.A.S. Smith, The emerging field of medicines authentication by nuclear quadrupole resonance spectroscopy, Appl. Magn. Reson. 43 (2012) 511–529.
- [38] C. Chen, F. Zhang, J. Barras, K. Althoefer, S. Bhunia, S. Mandal, Authentication of medicines using nuclear quadrupole resonance spectroscopy, IEEE/ACM Trans. Comput. Biol. Bioinf. 13 (2016) 417–430.
- [39] S.J. Seltzer, M.V. Romalis, Unshielded three-axis vector operation of a spin-exchange-relaxation-free atomic magnetometer, Appl. Phys. Lett. 85 (2004) 4804–4806.
- [40] G. Bevilacqua, V. Biancalana, Y. Dancheva, L. Moi, All-optical magnetometry for NMR detection in a micro-tesla field and unshielded environment, J. Magn. Reson. 201 (2009) 222–229.
- [41] D.A. Keder, D.W. Prescott, A.W. Conovaloff, K.L. Sauer, An unshielded radio-frequency atomic magnetometer with sub-femtotesla sensitivity, AIP Adv. 4 (2014) 127159, https://doi.org/10.1063/1.4905449.
- [42] G. Bevilacqua, V. Biancalana, P. Chessa, Y. Dancheva, Multichannel optical atomic magnetometer operating in unshielded environment, Appl. Phys. B 122 (2016) 1–9.
- [43] R.J. Cooper, D.W. Prescott, P. Matz, K.L. Sauer, N. Dural, M.V. Romalis, E.L. Foley, T.W. Kornack, M. Monti, J. Okamitsu, Atomic magnetometer multisensor array for RF interference mitigation and unshielded detection of nuclear quadrupole resonance, Phys. Rev. Appl. 6 (2016) 064014.
- [44] A. Corney, Atomic and Laser Spectroscopy, Oxford Science Publications, Clarendon Press, 1977.
- [45] R.J. Cooper, B.L. Mark, D.W. Prescott, K.L. Sauer, Improving the design of atomic magnetometer arrays for RF interference mitigation in NQR detection of explosives, in: Proc. SPIE, vol. 10182, 2017, p. 1018208.
- [46] W. Happer, B.S. Mathur, Off-resonant light as a probe of optically pumped alkali vapors, Phys. Rev. Lett. 18 (1967) 577–580.
- [47] V. Shah, G. Vasilakis, M.V. Romalis, High bandwidth atomic magnetometery with continuous quantum nondemolition measurements, Phys. Rev. Lett. 104 (2010) 013601.
- [48] D. Budker, D.F.J. Kimball, Optical Magnetometry, Optical Magnetometry, Cambridge University Press, 2013.
- [49] W. Happer, Y.Y. Jau, T. Walker, Optically Pumped Atoms, Wiley, 2010.
- [50] A. Abragam, Principles of Nuclear Magnetism, International Series of Monographs on Physics, Oxford University Press, 1983.
- [51] S. Appelt, A. Ben-Amar Baranga, C.J. Erickson, M.V. Romalis, A.R. Young, W. Happer, Theory of spin-exchange optical pumping of ³He and ¹²⁹Xe, Phys. Rev. A 58 (1998) 1412–1439.

- [52] C.P. Slichter, Principles of Magnetic Resonance, Springer Series in Solid-State
- Sciences, Springer, Berlin, Heidelberg, 1996.
 [53] Twinleaf LLC, 2017. http://www.twinleaf.com/.
 [54] D.K. Walter, W.M. Griffith, W. Happer, Energy transport in high-density spinexchange optical pumping cells, Phys. Rev. Lett. 86 (2001) 3264-3267.
- [55] B. Lancor, T.G. Walker, Effects of nitrogen quenching gas on spin-exchange optical pumping of ³He, Phys. Rev. A 82 (2010) 043417.
- [56] D. Chauvat, J. Guna, P.h. Jacquier, M. Lintz, M. A Bouchiat, M.D. Plimmer, C. W Goodwin, Magnification of a tiny polarisation rotation by a dichroic plate in balanced mode polarimetry, Opt. Commun. 138 (1997) 249–252.
- [57] Tecmag Inc., 2015. http://www.tecmag.com>.

- [58] O. Alem, Spin-Damping in an Ultra-Sensitive Tunable RF Atomic Magnetometer (Ph.D. thesis), George Mason University, 2011.
- [59] R.A. Marino, S.M. Klainer, Multiple spin echoes in pure quadrupole resonance, J. Chem. Phys. 67 (1977) 3388–3389.
- [60] R.S. Cantor, J.S. Waugh, Pulsed spin locking in pure nuclear quadrupole resonance, J. Chem. Phys. 73 (1980) 1054-1063, https://doi.org/10.1063/ 1.440277.
- [61] M.W. Malone, M. McGillvray, K.L. Sauer, Revealing dipolar coupling with NQR
- off-resonant pulsed spin locking, Phys. Rev. B 84 (2011) 214430.
 [62] D. Sheng, S. Li, N. Dural, M.V. Romalis, Subfemtotesla scalar atomic magnetometry using multipass cells, Phys. Rev. Lett. 110 (2013) 160802.